Mobility and conductivity of laser-generated *e-h* plasmas in direct-gap nanowires

Jeremy R. Gulley*, Rachel Cooper, Ethan Winchester

ᵃDepartment of Physics, Kennesaw State University, , Kennesaw, GA, 30144, USA

Abstract

This article examines the role of field strength, frequency, and many-body scattering during the ultrafast optoelectronic response in a direct-gap semiconductor nanowire using numerical simulation. Following resonant laser excitation, an AC or bias DC field perturbs the 1D *e-h* plasma as it relaxes by carrier-phonon and Coulomb scattering. For bias DC fields, the laser-excited carrier distributions evolve to a static non-equilibrium from which a stable DC mobility is calculated. Carrier-phonon collisions contain the *e-h* carriers near energy minima for fields of 0.5 kV/cm or less, while the Coulomb collisions redistribute some electrons across the Brillouin zone where they drift into other band structure energy minima and are there contained by phonon scattering. This behavior results in carrier mobilities with a field-strength dependence specific to a 1D solid. For AC probe fields, the analyze the resulting frequency-dependent conductivity for frequencies between the plasmon frequency and interband resonance. In all cases, we compare results to standard-conductivity models by calculating distribution-averaged collision rates and times, and show how, unlike in the bulk, these quantities for the nanowire are strongly dependent on both field magnitude and frequency.

Keywords: Quantum wires, Semiconductor, GaAs, Ultrashort laser, *e-h* plasma

1. Introduction

Semiconductor nanowires are of interest for many scientific and technological advances including in solar cells [1, 2], photovoltaics [3, 4], nanowire-based lasers [5–8], transistor designs [9–11], photodetectors [12, 13], THz-applications [14, 15], and numerous other optoelectronic applications [15, 16]. The behavior of electrons in a 1D nanoscale semiconductor is intrinsically quantum mechanical. In particular, the dimensionality of a solid strongly affects the optoelectronic properties of direct-gap semiconductors [10, 17–21]. For example, resonant optical transitions in a 3D direct-gap solid occur in a region near the Gamma point where the density of states (DOS) is approximately zero. Contrast this with Γ-point transitions in an analogous 2D solid, with a constant DOS, or in a 1D solid, with a DOS approaching infinity. During optical excitation and thermalization, dimensionality alters the optical response and electronic properties of the solid, even when calculations use the same fundamental models of electron-electron, electron-phonon, and electron-field interaction [16, 22–24]. Here, a 1D solid means only that the nanowire length $L \gg R_0$, where the nanowire radius $R_0 < 10$ nm is not large enough to justify the use of a continuous crystal momentum-space via Bloch's theorem in the transverse directions as we do for L along the nanowire axis.

For direct-gap semiconductor nanowires, optically excited near the Γ-point, the infinite DOS allows the electron and hole distributions to relax exclusively into the lowest excited energy states, eventually reaching a thermal equilibrium with the lattice. In bulk materials, however, these lowest excited energy

states are relatively few in number. Therefore, for high density plasmas, a nanowire can more effectively scatter carriers from higher energies to lower energies during many-body collisions then can a higher dimensional solid. This behavior is further complicated when a bias-DC or AC field keeps an excited carrier distribution from reaching equilibrium, causing a unique 1D optoelectronic response as measured by mobility and conductivity.

In this article, we simulate the excitation of a subwavelength GaAs nanowire by an ultrashort resonant laser pulse followed by relaxation under exposure to either a DC bias field or an AC probe field. After thermalization, the DC mobilities of electrons and holes are shown as nonlinear functions of DC field strength. We show field strength limits for meaningful definition of mobility for this system and use this as a basis for a comparison with frequency dependent AC conductivity calculations after the excited carriers are exposed to a AC probe pulse.

2. Theoretical model

Electron-hole dynamics in the crystal momentum space k of a 1D solid are modeled by the Semiconductor Bloch equations [19, 25, 26]. Under the diople approximation, the time evolution of the occupation numbers for electrons and holes, f_k^e and f_k^h, are given by

$$\frac{\partial f_k^{e,h}}{\partial t} = -2\,\text{Im}\left[\Omega_k P_k^*\right] + \frac{|e|\,E(t)}{\hbar}\nabla_k f_k^{e,h} + \frac{\partial f_k^{e,h}}{\partial t}\bigg|_{\text{scat}}. \quad (1)$$

In Eq. 1, the first term causes optical transitions from the valence to the conduction band, the second term causes *e-h* drift due to the external electric field $E(t)$, and the third term includes

---

*Jeremy R. Gulley
Email address:* `jgulley@kennesaw.edu` (Jeremy R. Gulley)

many-body scattering. In the first term, the microscopic polarization, P_k, is time evolved by

$$\frac{\partial P_k}{\partial t} = -\frac{i}{\hbar}\left(\varepsilon_k^e + \varepsilon_k^h + \mathcal{E}_{\text{Gap}} - i\,\hbar(\Gamma_k^e + \Gamma_k^h)\right)P_k \qquad (2)$$
$$+ i\Omega_k\left(1 - f_k^e - f_k^h\right) + \frac{|e|}{\hbar}E(t)\nabla_k P_k$$
$$+ \left(\Lambda_{k,q}^e + \Lambda_{k,q}^h\right)P_{k+q}.$$

In Eqs. 1 and 2, the generalized Rabi frequency, Ω_k, and renormalized single particle energies of the electrons and holes, $\varepsilon_k^{\text{e,h}}$, are given by:

$$\Omega_k = \frac{1}{\hbar}d_k^{cv}E(t) - \frac{1}{\hbar}\sum_{q\neq 0}V_q\,P_{k-q}. \qquad (3)$$

$$\varepsilon_k^{\text{e,h}} = \frac{1}{\hbar}\mathcal{E}_k^{\text{e,h}} - \frac{1}{\hbar}\sum_{q\neq 0}V_q\,f_{k-q}^{\text{e,h}}, \qquad (4)$$

Here, $\mathcal{E}_k^{\text{e,h}}$ are the single particle energies, V_q is the Fourier transform of the Coulomb potential matrix element, d_k^{cv} is the dipole matrix element, and $E(t)$ is the external electric field including the laser pump field and applied AC or DC fields. We note that while the corrections to the single particle energies and generalized Rabi frequencies have a minor effect on pump pulse excitation, they do not play a major role in presented AC and DC probe field responses. For a 1D system, the Coulomb potential may be approximated by $V_q = (e^2/2\pi\epsilon_0\epsilon_b)K_0(|q|R_0)$, where $K_0(x)$ is the zeroth order modified Bessel function of the second kind, R_0 is the nanowire radius, and ϵ_b is the background dielectric index [22, 27]. The dipole matrix elements d_k^{cv} are given by

$$d_k^{cv} = d_0^{cv}\,\frac{\varepsilon_0^{\text{e}} + \varepsilon_0^h + \mathcal{E}_{\text{Gap}}}{\varepsilon_k^{\text{e}} + \varepsilon_k^h + \mathcal{E}_{\text{Gap}}}, \qquad (5)$$

where d_0^{cv} is the dipole matrix element at the Γ-point, and $\mathcal{E}_{\text{Gap}}$ is the band gap energy [19].

The scattering term in Eq. 1 includes Coulomb scattering in the laser generated *e-h* plasma, as well as *e-h*-phonon scattering. Using the Markov approximation, this term is given by

$$\left.\frac{\partial f_k^{\text{e,h}}}{\partial t}\right|_{\text{scat}} = W_k^{\text{e,h(in)}}(1 - f_k^n) - W_k^{\text{e,h(out)}}f_k^n \qquad (6)$$

where the calculation of rates $W_k^{\text{e,h(in)}}$ and $W_k^{\text{e,h(out)}}$ are given in detail in the Appendix of Ref. [28]. Equation 2 includes Coulomb scattering effects under the Markov approximation in the diagonal dephasing rates, $\Gamma_k^{e,h}$, and off-diagonal dephasing rates, $\Lambda_{k,q}^{e,h}$. These too are detailed in the Appendix of Ref. [28]. The needed constants for these calculations are given in Tab. 1. These contributions act on the femtosecond time scale to relax the carriers toward a quasistatic non-equilibrium state [29]. We note that scattering terms in Ref. [28] additionally include spontaneous *e-h* recombination. We neglect that contribution in this work because the presented simulations cover less than 100 picoseconds in time duration, while the characteristic recombination times are on the order of nanoseconds or greater.

The solutions to Eq. 1 allow calculation of the free current density for electrons and holes $J_{\text{e,h}}(t)$ in the nanowire over time:

$$J_{\text{e,h}}(t) = \frac{-2|e|}{\text{Vol}}\sum_k f_k^{\text{e,h}}v_k^{e,h} \qquad (7)$$

where $v_k^n = \hbar^{-1}\partial_k\varepsilon_k^n$ is the carrier group velocity, the nanowire volume is $\text{Vol} = \delta_0^2\mathcal{L}$, the factor of 2 includes spin degeneracy, and the total current density is

$$J(t) = J_e(t) + J_h(t). \qquad (8)$$

At all times, the *e-h* carrier densities are given by

$$N_{\text{e,h}}(t) = \frac{2}{\text{Vol}}\sum_k f_k^{\text{e,h}}(t). \qquad (9)$$

Since we deal with a pure crystal in the absence of doping, we use $N_e(t) = N_h(t) = N(t)$. Furthermore, neglecting non-optical band transitions (*i.e.* impact ionization and Auger recombination), the carrier density $N(t)$ is a function of time only during excitation by the pump pulse, after which it remains constant, $N(t) \to N_c$. Restricting our measurements to post-excitation times, we define a charge-density-normalized conductivity $\mu_{\text{e,h}}(\omega)$ and relate it to the current density by

$$\mu_{\text{e,h}}(\omega) = \frac{1}{|e|N_c}\frac{\tilde{J}_{\text{e,h}}(\omega)}{\tilde{E}_{\text{pr}}(\omega)}, \qquad (10)$$

where $\tilde{E}_{\text{pr}}(t)$ is the Fourier transformed probe field. Here, $\mu_{\text{e,h}}(\omega)$ is relevant for both AC and DC fields, and in the DC limit $\mu_{\text{e,h}}(\omega = 0)$ becomes the carrier mobility.

In the Drude model, the normalized conductivity of carriers is given by $\mu_{\text{e,h}}(\omega) = |e|/m_{e,h}^*(\gamma_{\text{e,h}} - i\omega)$, where $\gamma_{\text{e,h}}$ is the collision rate and $m_{\text{e,h}}^*$ is the effective carrier mass at the Gamma point. Therefore, in the case of a DC probe field ($\omega = 0$) the Drude collision rate is

$$\gamma_{\text{e,h}} = \frac{|e|}{m_{\text{e,h}}^*\mu_n(0)}, \qquad (11)$$

while for AC probe fields the Drude rate is calculated from the real and imaginary parts of $\mu_{\text{e,h}}(\omega > 0)$ by

$$\gamma_{\text{e,h}} = \frac{\Re[\mu_{\text{e,h}}(\omega_0)]}{\Im[\mu_{\text{e,h}}(\omega_0)]}\omega_0, \qquad (12)$$

where ω_0 is the central frequency of $\tilde{E}_{\text{pr}}(\omega)$. We note that a Drude model for nanowires is not adequate to describe the low frequency range between $\omega = 0$ and the surface plasmon resonance frequencies [15], nor is that physics included in Eq.1 since intraband coherences are neglected [25]. For frequencies on the order of a THz or less, a normalized conductivity of $\mu_{\text{e,h}}(\omega) = (|e|i\omega/m_{e,h}^*)/(\omega^2 - \omega_{\text{e,h}}^2 + i\omega\gamma_{\text{eh}})$ is more applicable [15], where ω_{eh} is the plasmon resonance frequency. This model agrees well with the Drude model for $\omega \gg \omega_{\text{eh}}$, down to where the real and imaginary parts of $\mu_{\text{e,h}}(\omega)$ are approximately equal. Therefore, we restrict our AC results to this region, use Eq.12 to estimate γ for $\omega_0 \gg \omega_{\text{eh}}$, use Eq.10 results to estimate the frequency where $\Re[\mu_{\text{e,h}}(\omega_*)] \approx \Im[\mu_{\text{e,h}}(\omega_*)]$ and use $\omega_*^2 - \omega_{\text{eh}}^2 = \gamma\omega_*$ to estimate ω_{eh}.

Parmeter	Description	Value	Units
$\mathcal{E}_{Gap}$	Band gap	1.42[1]	eV
d_0^{cv}	Dipole matrix element at $k = 0$	0.73[2]	e nm
ϵ_s	Dielectric constant at $\omega = 0$	10.0[3]	
ϵ_∞	Dielectric constant at $\omega = \infty$	8.2[3]	
ϵ_b	Background dielectric constant	9.1[3]	
$\hbar\Omega_{ph}$	LO Phonon energy	36[3]	meV
$\hbar\Gamma_{ph}$	Inverse phonon lifetime	1[3]	meV
T	Background lattice temperature	77[4]	K
$\mathcal{L}$	Length of nanowire	565[5]	nm
δ_0	Thickness of nanowire	5.65[6]	nm

[1] Taken from the band structure in Fig. 1 [30].

[2] $d_0^{cv} = \sqrt{(3e^2\hbar^2/4m_0\mathcal{E}_{Gap})(m_0/m_e^* - 1)}$, $m_e^* = 0.07m_0$ [28].

[3] Values for GaAs nanowire embedded in a AlAs host [28].

[4] System cooled by liquid nitrogen.

[5] Simulations assume 1000 k−points in the BZ, making $\mathcal{L}$ 1000 unit cells long.

[6] Thickness of $\sim$ 10 unit cells.

Table 1: **Material parameters for simulations.**

3. Simulation

Equations 1-2 were solved numerically using a fourth-order Runge-Kutta routine with step sizes of 40-as and 20-as to ensure convergence. We take the nanowire crystal orientation to be aligned in the $\Gamma - X$ direction and use the bulk GaAs band structure from Ref. [30] to provide the single-particle energies $\mathcal{E}_k^n$, see Fig. 1. Table 1 summarizes all other material parameters used in the simulations. We justify using a bulk band structure for our 1D system as follows: The calculated band structures of GaAs nanowires vary widely in the literature, depending on crystal orientation, crystal structure (wurtzite or zinc blende), nanowire thickness, and the presence of impurities [31–33]. The e-h carrier dynamics in our simulations do not depend on the exact details of the band structure, but only on whether energy extrema exist between the gamma point and the Brillouin zone (BZ) edge. Specifically, it is the infinite DOS at these energy extrema causes the behavior of a 1D system to deviate from that of a bulk crystal. Therefore, our results are qualitatively valid regardless of specific band structure.

Figure 1 shows the band structure for the spin-orbit split-off (h_1), light-hole (h_2), and heavy-hole (h_3) sub-bands, as well as the first two conduction sub-bands (e_1 and e_2) [30]. We first solved the multi-band SBEs as given in Ref. [26] for our given conditions with the five sub-bands shown in Fig. 1. The h_1 and h_2 sub-bands are dipole coupled to e_1 for linearly polarized light [34], while all other dipole couplings are weak or forbidden. In these calculations appreciable excitation ($f_k^{e,h} \geq 0.1$) occurred only in sub-bands h_2 and e_1, justifying our two-band model in Eq. 1 and Eq. 2.

The total electric field $E(t)$ in Eqs. 1-3 is polarized along the nanowire axis and comprises the laser pump pulse $E_L(t)$ and the probe field $E_{pr}(t)$:
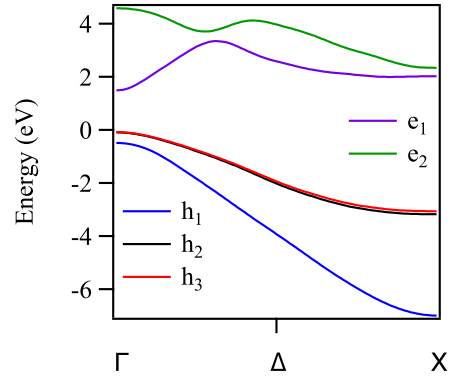

Figure 1: GaAs band structure used in the calculations [30]: split-off (h_1, blue), light-hole (h_2, black), heavy hole (h_3, red), first conduction (e_1, purple), and second conduction (e_2, green) bands. Only bands h_2 and e_1 contribute appreciably to the calculations presented.

$$E(t) = E_L(t) + E_{pr}(t), \tag{13}$$

$$E_L(t) = E_\ell \cos(\omega_\ell t) e^{-(t/\tau_\ell)^2}, \tag{14}$$

where $E_{pr}(t)$ is either a DC or an AC field given by

$$E_{pr}(t) = \begin{cases} E_{dc} \, f_{dc}(t), & \omega_0 = 0 \\ E_{ac} \cos(\omega_0 t) \, e^{-(t-t_{ac})^2/\tau_{ac}^2}, & \omega_0 > 0 \end{cases} \tag{15}$$

Here, ω_0 is again the central frequency of the probe field, and the function $f_{dc}(t)$ is a slow switch on function given by

$$f_{dc}(t) = \begin{cases} 1 - e^{-(t/\tau_{dc})^{12}} & , t < 0 \\ 1 & , t \geq 0. \end{cases} \tag{16}$$

The slow switch on of the DC field is meant to be half of a soft box function, for which we use a super Gaussian function of order six, centered about $t = 0$. Equation 16 ensures that the DC field is fully switched on before the pump pulse arrives. This same approach is not practical for the AC probe field, because while the DC field mobility is real (by definition), the AC conductivity is complex and requires numerical Fourier transforms of the calculated current density and AC probe field, see Eq. 10, which is not meaningful numerically unless both go to zero at $t = \pm\infty$. Therefore, we used an AC probe pulse spectrally centered at the frequency of interest and time-centered at $t = 20$ ps, after the e-h plasma has reached a static non-equilibrium state.

Table 2 summarizes all values appearing in Eqs. 14-16. Most values are constant for all simulations, but the probe field values of E_{dc}, λ_{ac}, and τ_{ac} are varied over ranges specified in the Tab 2. The pump wavelength is resonant with the nanowire bandgap, while its amplitude is high enough to excite an appreciable e-h plasma within the 20 fs pulsewidth. The range of AC probe wavelengths is nonresonant with the nanowire, and its amplitude is orders of magnitude below E_ℓ, so it does not excite new e-h pairs. We increase AC pulsewidths linearly with

Parmeter	Description	Value(s)	Units
E_ℓ	Pump amplitude	0.75	MV/cm
λ_ℓ	Pump wavelength[1]	800	nm
τ_ℓ	Pump pulsewidth[2]	20	fs
E_{dc}	DC field strength	0.01 - 1	kV/cm
τ_{dc}	DC switch-on time	5	ps
E_{ac}	AC probe amplitude	0.141	kV/cm
λ_{ac}	AC probe wavelength[1]	1.5 - 1500	μm
τ_{ac}	AC probe pulsewidth[2]	5 - 5000	fs
t_{ac}	AC probe delay	20	ps

[1] $\omega_\ell = 2\pi c / \lambda_\ell$ and $\omega_0 = 2\pi c / \lambda_0$.
[2] The $1/e^2$ pulsewidth.

Table 2: **Field parameters for simulations.**

wavelength, $\tau_{ac} = (33.3 \text{ fs}/\mu\text{m})\lambda_{ac}$, to keep the same temporal field form for each AC pulse. We also varied the DC field strengths to examine nonlinear effects.

Figure 2 shows a time schematic of the simulations. The resonant pump pulse is centred at the $t = 0$, exciting an *e-h* plasma in the nanowire. The probe field peak follows 20 ps later for the AC probe fields (see dashed black line); the DC field reaches its peak value prior to arrival of the pump pulse (solid black plot). The AC probe's 20 ps delay allows sufficient time for the excited *e-h* plasma to relax to a nonequilibrium steady-state.
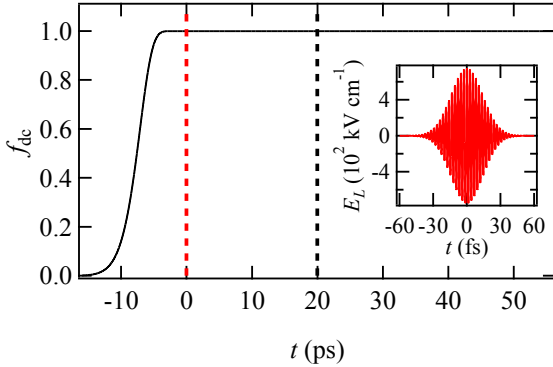

Figure 2: Time schematic of the simulations. The solid black line shows the DC slow switch-on function $f_{dc}(t)$, the dashed red line shows the laser pump pulse at $t = 0$, the dashed black line shows the center of the AC probe field at $t = 20$ ps, and the inset zooms in on the laser pump pulse.

4. DC Probe Field Results

The DC probe field simulations assumed field strengths ranging from 0.01-1.0 kV/cm. The presence of these DC fields did not significantly impact the optical excitation from the pump pulse, either in the total number of carriers generated or in their initial momentum distributions. This is because the pump pulse lasted only tens of femtoseconds while the comparatively smaller DC fields modified the distributions appreciably over picoseconds. To characterize the role of many-body effects in
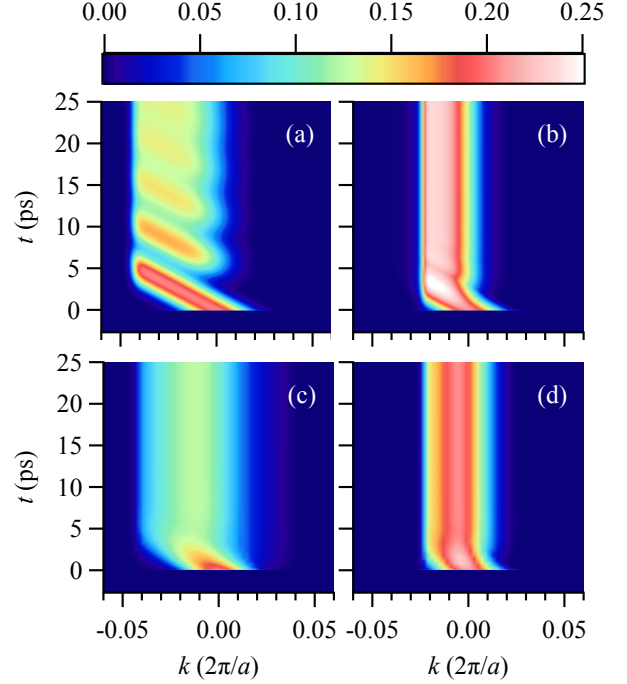

Figure 3: The hole (a, c) and electron (b, d) occupation numbers (f_k^h, f_k^e) as functions of k and t. The pump pulse is incident at $t = 0$ along with a DC field of $E_{dc} = 0.5$ kV/cm. Plots (a, b) include only phonon scattering in Eq. 6; plots (c, d) include phonon scattering and Coulomb collisions in Eq. 6.

the *e-h* mobility, one set of simulations included only carrier-phonon collisions in Eq. 6 and another set included both carrier-phonon and Coulomb collisions. The occupation numbers $f_k^h(t)$ and $f_k^e(t)$ were recorded (Fig. 3), and once these distributions reach a non-equilibrium steady-state, the current densities (Fig. 4), carrier mobilities (Fig. 5), and collision rates (Fig. 6) were calculated according to Eqs. 7, 10, and 11, respectively.

4.1. The role of carrier-phonon collisions

Figure 3(a,b) shows the distributions $f_k^h(t)$ and $f_k^e(t)$ for $E_{dc} = 0.5$ kV/cm. After excitation at $t = 0$, the DC field shifts the *e-h* distributions in k-space over time. The carriers accelerate until they reach the crystal momentum $k_{ph}^{e,h}$ associated with the characteristic phonon energy, $\mathcal{E}_{k_{ph}^{e,h}}^{e,h} = \hbar\Omega_{ph}$, at which point carrier-phonon scattering returns carriers from $k \approx k_{ph}^{e,h}$ to $k \approx 0$. This process then repeats periodically, see Fig. 3(a,b), until a non-equilibrium steady-state results. The oscillations are more apparent in the hole distribution (Fig. 3a) than in the electron distribution (Fig. 3b) because electrons accelerate to momentum k_{ph}^e sooner than the holes accelerate to k_{ph}^h.

Figure 4(a) shows the total current densities for simulations using different DC field strengths. The temporal periodicity of $f_k^h(t)$ in Fig. 3a causes corresponding oscillations in the total current density over time, see the solid black line in Fig. 4(a). Note that for $E_{dc} \leq 0.5$ kV/cm, all currents eventually converge to a single value. Fig 3(a,b) shows the cause of this current density cutoff effect; the resulting non-equilibrium distributions settle at values approaching $k \approx k_{ph}^{e,h}$, regardless of DC field
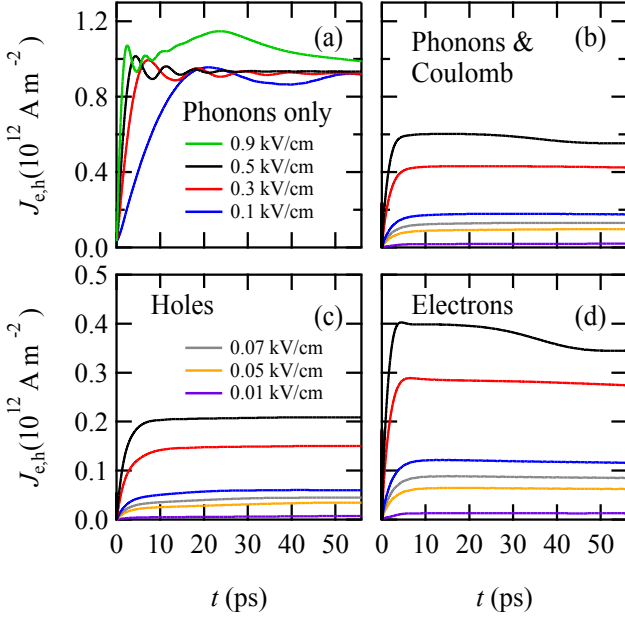
Figure 4: The total current densities including only phonon scattering (a) or both phonon and Coulomb scattering (b) in Eq. 6. Plots (c, d) show the individual hole (c) and electron (d) current densities with both phonon and Coulomb scattering in Eq. 6. All plots show results for varying DC field strengths, for which the legend is split between (a) and (c), but applies to all plots.
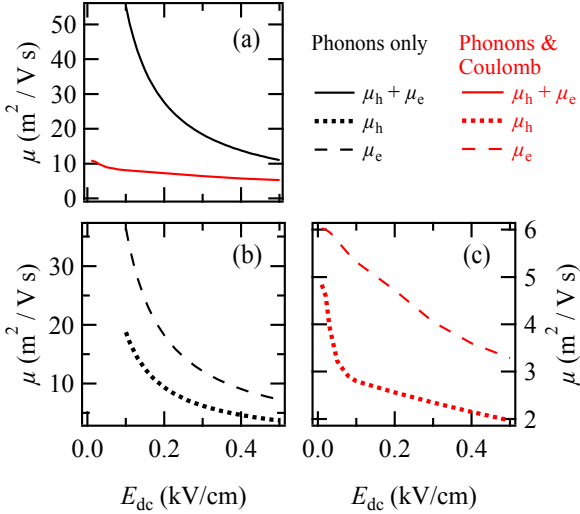

Figure 5: The nonlinear carrier mobilities as a function of applied DC field E_{dc} shown for simulations including only carrier-phonon collisions (black plots) and both phonon and Coulomb collisions (red plots). (a) shows the total mobilities in both cases, (b) and (c) show the individual electron and hole mobilities for both cases.

strength. In these cases with only carrier-phonon scattering, the time required to reach a steady-state scales inversely with E_{dc}. We expect this trend to hold for all lower field strengths, yielding mobilities and collision times approaching infinity as $E_{dc} \rightarrow 0$. Hence, we restrict the phonon-scattering-only data in Figs. 3-6 to values $E_{dc} \geq 0.1$ kV/cm.
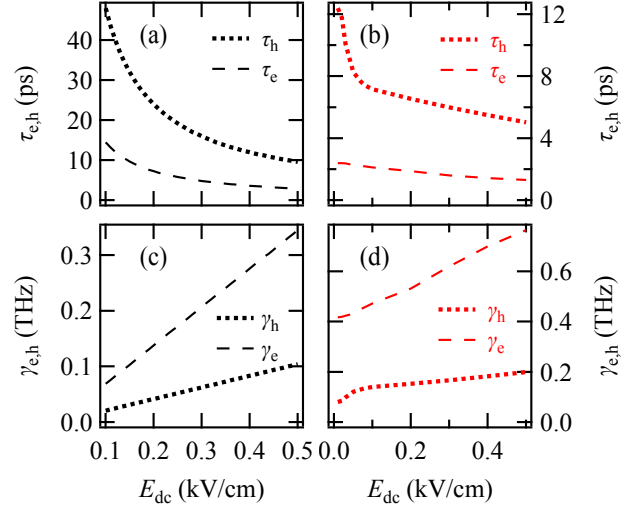

Figure 6: The distribution-averaged collision times (a,b) and rates (c,d) of electrons (dashed lines) and holes (dotted lines) for simulations including only phonon collisions (a,c) or both phonon and Coulomb collisions (b,d) as functions of E_{dc}.

In our simulations, the threshold effect on the carriers and their currents did not hold for $E_{dc} > 0.5$ kV/cm, beyond which a small but appreciable percentage of carriers accelerate past $k_{ph}^{e,h}$ before scattering events can relax the distribution. This causes currents that do not converge to the low E_{dc} current values, see green line in Fig. 4(a). Thus, we do not include $E_{dc} > 0.5$ kV/cm in further simulations since they do not allow for a steady state solution from which we can calculate a meaningful mobility.

The black plots in Fig. 5 show the total DC mobility (a) and individual electron and hole DC mobilities (b) including only phonon scattering in Eq. 6. As expected, these mobilities scale as $1/E_{dc}$, as electrons spend more time traveling between $k \approx 0$ and $k \approx k_{ph}^{e,h}$, with near zero resistance, as $E_{dc} \rightarrow 0$. Figure 6 (a,c) shows the distribution-averaged collision rates (c) and collision times (a) calculated by $\tau_n = 1/\gamma_n$. For the DC case, the collision time is mathematically proportional to mobility. Hence, $\tau_{e,h}$ scales as $1/E_{dc}$ in Fig. 5a while $\gamma_{e,h}$ in Fig. 5 c is linear with E_{dc}.

This behavior is seemingly unphysical. The mobility values of 1-10 m^2/(V s) approximate those of bulk GaAs, but the bulk material does not exhibit such a field dependence. Our model is 1D, but this behavior could still occur for low e-h densities in 2D or 3D if only carrier-phonon collisions are included in Eq. 6. For example, a spherical $f_k^{e,h}$ in a 3D k-space would still accelerate until carriers reach the boundary of a larger sphere defined by the radius $k \approx k_{ph}^{e,h}$. For low e-h densities, all carriers drifting into this boundary would scatter to $k \approx 0$ before accelerating again, creating an effective 1D distribution along the k-axis aligned with E_{dc}. For high carrier densities, the behavior would exhibit stronger dimensional dependence with the changing DOS of near-zero energy states that participate in scattering; infinity, constant, or zero for 1D, 2D, or 3D, respectively. Only

in the case of a 1D solid does the DOS guarantee a large surplus of states near $\varepsilon_{k=0}^{e,h}$ than near $\varepsilon_{k_{ph}^{e,h}}^{e,h}$. A 1D material could, therefore, maintain this behavior even for high carrier densities. The question now becomes, does this unusual 1D behavior survive the inclusion of Coulomb collisions in Eq. 6?

4.2. The role of Coulomb collisions

Figure 3(c,d) shows the e-h distributions over time when exposed to a DC field of $E_{dc} = 0.5$ kV/cm where Eq. 6 includes both carrier-phonon and Coulomb collisions. Figure 4(c,d) shows the individual hole and electron currents (Eq. 7) for these simulations at varying E_{dc} strengths, while Fig. 4b shows the corresponding total e-h currents (Eq. 8) for direct comparison with Figure 4a. For the simulations including Coulomb collisions, we performed simulations for E_{dc} down to 0.01 kV/cm to verify low field behavior. From these results, we observe that Coulomb collisions (a) more quickly relax the distributions to a non-equilibrium steady-state, (b) lead to high-E_{dc} electron currents that do not converge to a steady-state value on the same time scales as lower-E_{dc} or phonon-only currents, and (c) Coulomb collisions restore a near linear E_{dc} field dependence to the current density (as one expects physically). We discuss these facts and their implications below.

The Coulomb collisions seem to act quickly (less than 5 ps) to relax the distributions in Fig. 3(c,d) to a non-equilibrium steady-state. There is no consolidated periodic drifting of the holes in Fig. 3c, as there is in Fig. 3a. Thus, no corresponding oscillations appear in the electron and hole current densities, Fig. 4(c,d), or in their combined total current density, Fig. 4b, for any E_{dc} value. Coulomb collisions uniquely impact the higher E_{dc} dynamics, as shown by the electron current for $E_{dc} = 0.5$ kV/cm in Fig. 4d (black curve). Unlike the phonon-only currents in Fig. 4a, which converge to a steady-state value for $E_{dc} \leq 0.5$ kV/cm, the black curve in Fig. 4d appears to reach a steady value between $t = 5 - 20$ ps before declining until $t = 50$ ps. The cause of this behavior is not apparent on the linear-scale plots in Fig. 3d, which is why this figure stops at $t = 25$ ps (no further changes are visible beyond 25 ps). However, log scale plots of Fig. 3(c,d) reveal additional dynamics across the BZ that alter the resulting currents.

Figure 7(c,d) shows log plots of Fig. 3(c,d) covering the complete BZ, and for times up to 100 ps. For comparison with low field results, Fig. 7(a,b) shows the same plots but for $E_{dc} = 0.01$ kV/cm. For both high and low DC fields, Coulomb collisions scatter electrons, Fig. 3 (b,d) across the BZ, while holes, Fig. 3(a,c), remain near $k = 0$. The delayed electron scattering is due to our assumed band structure in Fig. 1. Coulomb collisions scatter some electrons away from $k = 0$ beyond $|k| > k_{ph}^{e}$, so that electrons with momentum $k < -|k_{ph}^{e}|$ then drift to an energy maximum at $k \approx -0.3(2\pi/a)$, arriving there between 25-50 ps. Additional collisions then scatter electrons to the vicinities of other band extrema near the BZ edge, where the velocities are near zero thus reducing the electron current. These pockets of electrons consolidate around the energy minimum at the BZ edge and the electrons everywhere relax to a steady-state. While this is the case for both low (Fig. 3a) and high
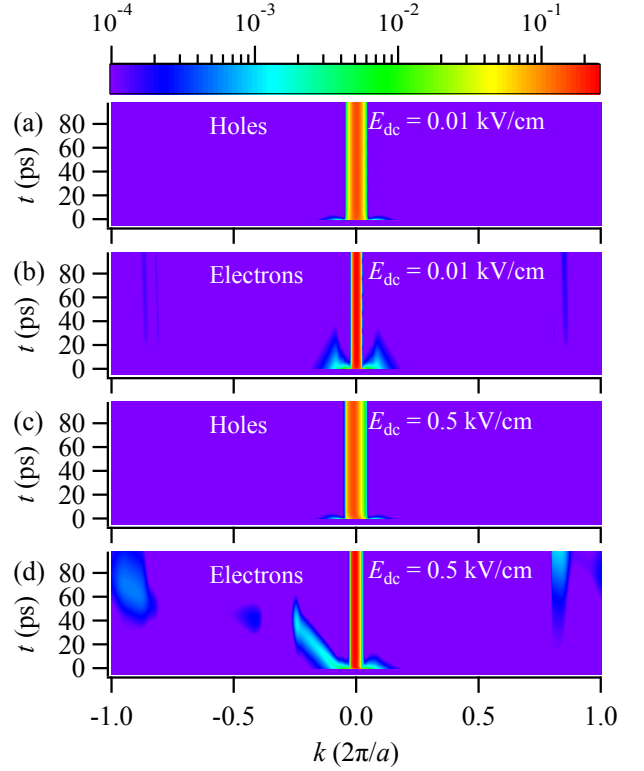

Figure 7: Log plots of f_k^h (a, c) and f_k^e (b, d) as functions of k and t, shown for $E_{dc} = 0.01$ kV/cm (a,b) and $E_{dc} = 0.5$ kV/cm (c,d). Results include phonon scattering and Coulomb collisions in Eq. 6 and are shown over the complete BZ.

(Fig. 3c) DC field simulations, a higher DC field leads to more electrons scattering past k_{ph}^{e} initially, and thus takes longer to reach a steady-state. The band structure for the holes, with extrema only at $k = 0$ and the BZ edge, prevents a similar behavior from occurring. The presence of multiple extrema is more significant in a 1D system, due to the near-infinite DOS there. Thus, this behavior is less likely to manifest in multiple dimensions.

Figure. 4(a,c) shows the total (a), and individual e-h mobilities (c) with phonon and Coulomb collisions. Comparison of the black and red plots in Fig. 4(a) demonstrates that Coulomb collisions restore a more physically intuitive field-dependence to the current density, albeit still a nonlinear dependence. The individual hole mobilities, dotted line in Fig. 4(c), show two distinct nonlinear regimes; for DC fields greater than or less than 0.07 kV/cm. This effect is understood when examining the resulting collision times and rates in Fig. 6 (b,d). Fig. 6 (b) suggests that a collision time of about 12-13 ps is the $E_{dc} = 0$ limit for holes, meaning that this is how approximately long it takes for Coulomb collisions to scatter the laser-generated carriers into states near energy $\hbar\Omega_{ph}$. This is the dominant mechanism of hole scattering for $E_{dc} < 0.07$ kV/cm, whereas for $E_{dc} > 0.07$ kV/cm the field induced drifting of holes plays an appreciable role. The electrons do not show this behavior because Coulomb collisions already scatter some carriers near and beyond $k = |k_{ph}^{e}|$, regardless of DC field strength. Thus, the elec-
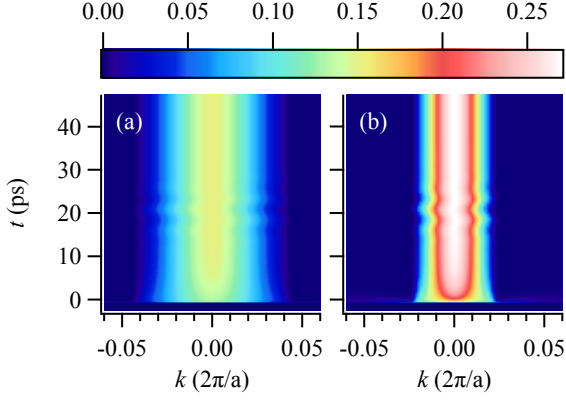
6

Figure 8: The hole (a) and electron (b) occupation numbers (f_k^h and f_k^e) as functions of k and t. The pump pulse is incident at $t = 0$ followed by an AC probe field centered at $t = 20$ ps (shown here for a probe wavelength of 1500 μm). Both phonon scattering and Coulomb collisions are included.

trons' behavior is complicated for high E_{dc}, and holes for low E_{dc}.

5. AC probe fields

To test the AC response of the 1D *e-h* plasma, we ran simulations using AC fields with a peak magnitude of $E_{ac} = 0.141$ kV/cm, such that the RMS value is comparable to the $E_{dc} = 0.1$ kV/cm simulations. Given that surface plasmon resonances are on the order of a THz, and that we must to avoid exciting additional resonant interband transitions, we limit the AC simulations to non-resonant probe wavelengths ranging from 1.5 - 1500 μm. For the 1500 μm wavelength case, Fig. 8 shows the hole and electron occupation numbers as functions of momentum k and time t with all phonon scattering and Coulomb collisions included. Note that the carriers are created at $t = 0$ by the original pump pulse, while the AC probe field that follows is centered about $t = 20$ ps, causing the generated carriers to oscillate over time in k-space. The meaningful quantity for AC fields is the conductivity, and since the total *e-h* densities are constant after excitation, we examine at the frequency-dependent, density-normalized conductivity, Eq. 10, and make direct comparison to the DC mobilities.

Fig. 9 shows the normalized conductivities $\mu_{e,h}(\omega)$ as well as the the *e-h* collision rates, Eq. 12, and corresponding collision times calculated for simulations with different AC probe frequencies. For added clarity, the figure displays the frequency dependence on the linear scale, Fig. 9(a,c,e), and log scale, Fig. 9(b,d,f). Both Drude and plasmon resonance models of $\mu_{e,h}(\omega)$ predict that its imaginary part will dominate at high frequency, which Fig. 9(a,b) confirms. As ω_0 decreases and approaches the THz regime, the real and imaginary parts of $\mu_{e,h}(\omega)$ should cross. Figure 9(a,b) confirms that this occurs in a region of $\omega_0 \approx 1$ THz. Combining this with the high frequency estimates for γ_{eh} in Fig.9(c,d) yields estimates for the electron and hole plasmon resonance frequencies of $\omega_e = 0.3$ THz and $\omega_h = 0.45$ THz.
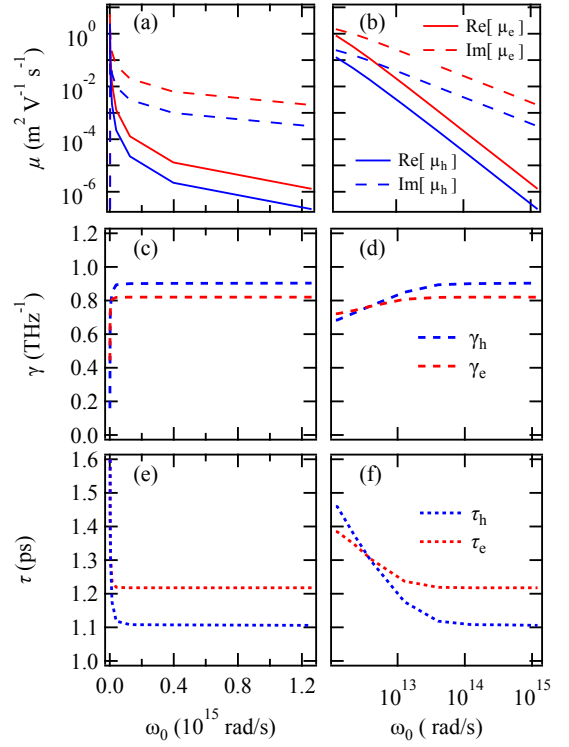

Figure 9: The individuial *e-h* (a) normalized conductivities, (c) Drude collision rates, and (e) Drude collision times as functions probe frequency ω_0. Plots (b,d,f) are the same as plots (a,c,e), but on a logarithmic ω_0 scale. Plots (a) and (b) show both real and imaginary parts of $\mu_{e,h}(\omega)$ on a log scale.

Generally, the conductivity of the electrons is higher than the holes due to the hole's larger effective mass near the Gamma point. To see non-Drude-like behavior even for $\omega \gg \omega_{e,h}$ we plot collision rates and times in Fig. 9(c-d). Between $\omega_0 \gg \omega_{e,h}$ and $\omega_0 < \omega_\ell$, collision rates $\gamma_{e,h}(\omega_0)$ vary about $\pm 15\%$ from 0.8 THz, whereas a Drude-type model does not typically assume a frequency dependent collision rate. This behavior results from the low-ω_0 AC fields driving the carriers in k-space further from the Gamma point during each field oscillation. Since the electrons experience less variability of scattering by phonon and Coulomb collisions at low field strengths (see DC results), the hole collision rates and times exhibit greater variability as AC frequency decreases. As with the DC case, this effect is more significant for a 1D solid, compared to bulk, due to the high DOS near the Gamma point.

6. Conclusion

In this article we used numerical simulation to examine the role of field strength, many-body scattering, and frequency during the ultrafast optoelectronic response in a GaAs nanowire after excitation by an ultrashort pump pulse. After photoexcitation, the laser-generated *e-h* plasma was perturbed by an AC or bias DC field. Our findings are that (a) For DC bias fields, carrier-phonon collisions contain the *e-h* carriers near band structure energy minima for fields of 0.5 kV/cm or less.

(b) In the absence of Coulomb collisions, the DC electronic response is eventually to converge to a single current value regardless of the bias voltage; an unphysical result. (c) Further inclusion of Coulomb collisions restore a near linear DC response as measured by carrier mobility and collision rates. (d) The AC electronic response deviates from a Drude-type response through frequency dependence of the mobility and collision rates as the AC frequency varies between THz and IR regimes. (e) In all cases, calculated distribution-averaged e-h collision times and rates show that, unlike in a bulk solid, these quantities in a nanowire are strongly field dependent, both on amplitude and frequency.

Acknowledgements

References

[1] B. Wang, E. Stevens, P. W. Leu, Strong broadband absorption in gaas nanocone and nanowire arrays for solar cells, Opt. Express 22 (S2) (2014) A386–A395. doi:10.1364/OE.22.00A386.
URL http://opg.optica.org/oe/abstract.cfm?URI=oe-22-102-A386

[2] J. Kupec, R. L. Stoop, B. Witzigmann, Light absorption and emission in nanowire array solar cells, Opt. Express 18 (26) (2010) 27589–27605. doi:10.1364/OE.18.027589.
URL http://www.opticsexpress.org/abstract.cfm?URI=oe-18-26-27589

[3] N. I. Goktas, P. Wilson, A. Ghukasyan, D. Wagner, S. McNamee, R. R. LaPierre, Nanowires for energy: A review, Appl. Phys. Rev. 5 (4) (2018) 041305. doi:10.1063/1.5054842.
URL https://doi.org/10.1063/1.5054842

[4] S. Mokkapati, C. Jagadish, Review on photonic properties of nanowires for photovoltaics, Opt. Express 24 (15) (2016) 17345–17358. doi:10.1364/OE.24.017345.
URL http://www.opticsexpress.org/abstract.cfm?URI=oe-24-15-17345

[5] Y. Ma, X. Guo, X. Wu, L. Dai, L. Tong, Semiconductor nanowire lasers, Adv. Opt. Photon. 5 (3) (2013) 216–273. doi:10.1364/AOP.5.000216.
URL https://opg.optica.org/aop/abstract.cfm?URI=aop-5-3-216

[6] R. Yi, X. Zhang, C. Li, B. Zhao, J. Wang, Z. Li, X. Gan, L. Li, Z. Li, F. Zhang, L. Fang, N. Wang, P. Chen, W. Lu, L. Fu, J. Zhao, H. H. Tan, C. Jagadish, Self-frequency-conversion nanowire lasers, Light, Sci. Appl. 11 (1) (2022) 120. doi:10.1038/s41377-022-00807-7.
URL https://doi.org/10.1038/s41377-022-00807-7

[7] M. F. Vafadar, S. Zhao, Ultralow threshold surface emitting ultraviolet lasers with semiconductor nanowires, Sci. Rep. 13 (1) (2023) 6633. doi:10.1038/s41598-023-33457-9.
URL https://doi.org/10.1038/s41598-023-33457-9

[8] S. W. Eaton, A. Fu, A. B. Wong, C.-Z. Ning, P. Yang, Semiconductor nanowire lasers, Nat. Rev. Mater. 1 (6) (2016) 16028. doi:10.1038/natrevmats.2016.28.
URL https://doi.org/10.1038/natrevmats.2016.28

[9] L. Balaghi, S. Shan, I. Fotev, F. Moebus, R. Rana, T. Venanzi, R. Hübner, T. Mikolajick, H. Schneider, M. Helm, A. Pashkin, E. Dimakis, High electron mobility in strained gaas nanowires, Nat. Commun. 12 (1) (2021) 6642. doi:10.1038/s41467-021-27006-z.
URL https://doi.org/10.1038/s41467-021-27006-z

[10] L. Samuelson, M. Björk, K. Deppert, M. Larsson, B. Ohlsson, N. Panev, A. Persson, N. Sköld, C. Thelander, L. Wallenberg, Semiconductor nanowires for novel one-dimensional devices, Phys. E: Low-Dimens. Syst. Nanostructures 21 (2) (2004) 560–567. doi:https://doi.org/10.1016/j.physe.2003.11.072.
URL doi:10.1016/j.physe.2003.11.072

[11] J. Appenzeller, J. Knoch, M. T. Bjork, H. Riel, H. Schmid, W. Riess, Toward nanowire electronics, IEEE Trans. Electron Devices 55 (11) (2008) 2827–2845. doi:10.1109/TED.2008.2008011.

[12] Z. Li, L. Li, F. Wang, L. Xu, Q. Gao, A. Alabadla, K. Peng, K. Vora, H. T. Hattori, H. H. Tan, C. Jagadish, L. Fu, Investigation of light-matter interaction in single vertical nanowires in ordered nanowire arrays, Nanoscale 14 (9) (2022) 3527. doi:10.1039/D1NR08088A.
URL http://dx.doi.org/10.1039/D1NR08088A

[13] F. Lin, J. Cui, Z. Zhang, Z. Wei, X. Hou, B. Meng, Y. Liu, J. Tang, K. Li, L. Liao, Q. Hao, Gaas nanowire photodetectors based on au nanoparticles modification, Materials 16 (4) (2023) 1735. doi:10.3390/ma16041735.
URL https://www.mdpi.com/1996-1944/16/4/1735

[14] H. B. Zhuo, S. J. Zhang, X. H. Li, H. Y. Zhou, X. Z. Li, D. B. Zou, M. Y. Yu, H. C. Wu, Z. M. Sheng, C. T. Zhou, Terahertz generation from laser-driven ultrafast current propagation along a wire target, Phys. Rev. E 95 (2017) 013201. doi:10.1103/PhysRevE.95.013201.
URL https://link.aps.org/doi/10.1103/PhysRevE.95.013201

[15] H. J. Joyce, J. L. Boland, C. L. Davies, S. A. Baig, M. B. Johnston, A review of the electrical properties of semiconductor nanowires: insights gained from terahertz conductivity spectroscopy, Semicond. Sci. Technol. 31 (10) (2016) 103003. doi:10.1088/0268-1242/31/10/103003.
URL https://dx.doi.org/10.1088/0268-1242/31/10/103003

[16] Z. Wang, B. Nabet, Nanowire optoelectronics, Nanophotonics 4 (4) (2015) 491–502. doi:doi:10.1515/nanoph-2015-0025.
URL file:///.file/id=6571367.8659761901

[17] G. Bastard, Wave mechanics applied to semiconductor heterostructures, les editions de physique, 1992.

[18] G. Gumbs, D. Huang, Properties of Interacting Low-Dimensional Systems, John Wiley & Sons, 2011.

[19] H. Haug, S. W. Koch, Quantum Theory of the Optical and Electronic Properties of Semiconductors, 5th Edition, World Scientific Publishing Co. Pte. Ltd., 2009.

[20] P. Harrison, Quantum Wells Wires and Dots: Theoretical and Computational Physics of Semiconductor Nanostructures, 2nd Edition, John Wiley & Sons, LTD, 2005.

[21] L. Samuelson, C. Thelander, M. Björk, M. Borgström, K. Deppert, K. Dick, A. Hansen, T. Mårtensson, N. Panev, A. Persson, W. Seifert, N. Sköld, M. Larsson, L. Wallenberg, Semiconductor nanowires for 0d and 1d physics and applications, Phys. E: Low-Dimens. Syst. Nanostructures 25 (2) (2004) 313–318. doi:https://doi.org/10.1016/j.physe.2004.06.030.
URL https://doi.org/10.1016/j.physe.2004.06.030

[22] S. Das Sarma, E. H. Hwang, Dynamical response of a one-dimensional quantum-wire electron system, Phys. Rev. B 54 (1996) 1936–1946. doi:10.1103/PhysRevB.54.1936.
URL https://link.aps.org/doi/10.1103/PhysRevB.54.1936

[23] X. Lu, D. Huang, J. R. Gulley, Laser-controlled ultrafast nonlinear optical responses of interacting e–h pairs in electromagnetically coupled GaAs quantum dots, J. Appl. Phys. 131 (7) (2022) 073101. arXiv:https://doi.org/10.1063/5.0081067, doi:10.1063/5.0081067.
URL https://doi.org/10.1063/5.0081067

[24] S. Aqiqi, C. Duque, A. Radu, J. Gil-Corrales, A. Morales, J. Vinasco, D. Laroze, Optical properties and conductivity of biased gaas quantum dots, Phys. E: Low-Dimens. Syst. Nanostructures 138 (2022) 115084. doi:https://doi.org/10.1016/j.physe.2021.115084.
URL https://www.sciencedirect.com/science/article/pii/S1386947721004392

[25] J. R. Gulley, D. Huang, Ultrafast transverse and longitudinal response of laser-excited quantum wires, Opt. Express 30 (6) (2022) 9348–9359. doi:10.1364/OE.448934.
URL http://opg.optica.org/oe/abstract.cfm?URI=oe-30-6-9348

[26] O. Schubert, M. Hohenleutner, F. Langer, B. Urbanek, C. Lange, U. Huttner, D. Golde, T. Meier, M. Kira, S. W. Koch, R. Huber, Sub-cycle control of terahertz high-harmonic generation by dynamical bloch oscillations, Nat. Photon. 8 (2) (2014) 119–123.
URL http://dx.doi.org/10.1038/nphoton.2013.349

[27] Q. P. Li, S. Das Sarma, Elementary excitation spectrum of one-dimensional electron systems in confined semiconductor structures: Zero magnetic field, Phys. Rev. B 43 (1991) 11768–11786.

doi:10.1103/PhysRevB.43.11768.
URL https://link.aps.org/doi/10.1103/PhysRevB.43.11768

[28] J. R. Gulley, D. Huang, Self-consistent quantum-kinetic theory for interplay between pulsed-laser excitation and nonlinear carrier transport in a quantum-wire array, Opt. Express 27 (12) (2019) 17154–17185. doi:10.1364/OE.27.017154.
URL http://www.opticsexpress.org/abstract.cfm?URI=oe-27-12-17154

[29] K. Huthmacher, A. K. Molberg, B. Rethfeld, J. R. Gulley, A split-step method to include electron–electron collisions via monte carlo in multiple rate equation simulations, J. Comput. Phys. 322 (2016) 535 – 546. doi:http://dx.doi.org/10.1016/j.jcp.2016.06.043.
URL http://www.sciencedirect.com/science/article/pii/S0021999116302686

[30] I. Vurgaftman, J. R. Meyer, L. R. Ram-Mohan, Band parameters for iii–v compound semiconductors and their alloys, J. Appl. Phys. 89 (11) (2001) 5815–5875. arXiv:https://doi.org/10.1063/1.1368156, doi:10.1063/1.1368156.
URL https://doi.org/10.1063/1.1368156

[31] S. Cahangirov, S. Ciraci, First-principles study of gaas nanowires, Phys. Rev. B 79 (2009) 165118. doi:10.1103/PhysRevB.79.165118.
URL https://link.aps.org/doi/10.1103/PhysRevB.79.165118

[32] Y. Diao, L. Liu, S. Xia, S. Feng, F. Lu, The electronic and optical properties of cs adsorbed gaas nanowires via first-principles study, Phys. E: Low-Dimens. Syst. Nanostructures 101 (2018) 5–10. doi:https://doi.org/10.1016/j.physe.2018.03.011.
URL https://www.sciencedirect.com/science/article/pii/S1386947718301966

[33] L. Pengfei, C. Huawei, Z. Xianlong, Y. Zhongyuan, C. Ningning, G. Tao, W. Shumin, Structural properties and energetics of gaas nanowires, Phys. E: Low-Dimens. Syst. Nanostructures 52 (2013) 34–39. doi:https://doi.org/10.1016/j.physe.2013.03.025.
URL https://www.sciencedirect.com/science/article/pii/S1386947713000945

[34] I. Kilen, M. Kolesik, J. Hader, J. V. Moloney, U. Huttner, M. K. Hagen, S. W. Koch, Propagation induced dephasing in semiconductor high-harmonic generation, Phys. Rev. Lett. 125 (2020) 083901. doi:10.1103/PhysRevLett.125.083901.
URL https://link.aps.org/doi/10.1103/PhysRevLett.125.083901